Cross-Shock Potential in Rippled vs. Planar Quasi-Perpendicular Shocks Observed by MMS

E.L.M. Hanson, O. V. Agapitov, F. S. Mozer, V. Krasnoselskikh, S.D Bale, L. Avanov, Y. Khotyaintsev, B. Giles

Geophysical Research Letters

RESEARCH LETTER
10.1029/2018GL080240

Cross-Shock Potential in Rippled Versus Planar Quasi-Perpendicular Shocks Observed by MMS

E. L. M. Hanson[1], O. V. Agapitov[1], F. S. Mozer[1], V. Krasnoselskikh[1,2], S. D. Bale[1], L. Avanov[3,4], Y. Khotyaintsev[5], and B. Giles[4]

[1]Space Sciences Laboratory, University of California, Berkeley, CA, USA, [2]LPC2E/CNRS-University of Orleans, Orléans, France, [3]Astronomy Department, University of Maryland, College Park, MD, USA, [4]NASA/Goddard Space Flight Center, Greenbelt, MD, USA, [5]Swedish Institute of Space Physics, Uppsala, Sweden

Key Points:
- We compared cross-shock potential structure of two quasi-perpendicular shocks (low/high Mach) in Magnetospheric Multiscale mission data
- The Normal Incidence Frame cross-shock potential was 26 +/- 6 V for low-Mach shock, 290-440 V for high-Mach shock, similar to electron proxies
- At the high-Mach shock, ion proxies were spoiled by ions reflected off the rippled front

Supporting Information:
- Supporting Information S1
- Supporting Information S2

Correspondence to:
E. L. M. Hanson,
lily.hanson@berkeley.edu

Citation:
Hanson, E. L. M., Agapitov, O. V., Mozer, F. S., Krasnoselskikh, V., Bale, S. D., Avanov, L., et al. (2019). Cross-shock potential in rippled versus planar quasi-perpendicular shocks observed by MMS. *Geophysical Research Letters*, *46*, 2381–2389. https://doi.org/10.1029/2018GL080240

Received 27 AUG 2018
Accepted 12 FEB 2019
Accepted article online 14 FEB 2019
Published online 14 MAR 2019

Abstract The unprecedented detail of measurements by the four Magnetospheric Multiscale (MMS) spacecraft enable deeper investigation of quasi-perpendicular collisionless shocks. We compare shock normals, planarities, and Normal Incidence Frame cross-shock potentials determined from electric field measurements and proxies, for a subcritical interplanetary shock and a supercritical bow shock. The subcritical shock's cross-shock potential was 26±6 V. The shock scale was 33 km, too short to allow comparison with proxies from ion moments. Proxies from electron moments provided potential estimates of 40±5 V. Shock normals from magnetic field minimum variance analysis were nearly identical, indicating a planar front. The supercritical shock's cross-shock potential was estimated to be from 290 to 440 V from the different spacecraft measurements, with shock scale 120 km. Reflected ions contaminated the ion-based proxies upstream, whereas electron-based proxies yielded reasonable estimates of 250±50 V. Shock normals from electric field maximum variance analysis differed, indicating a rippled front.

Plain Language Summary An important problem in shock physics is understanding how the incoming plasma flow is thermalized across the shock. The role of the cross-shock electric field has not been well studied. We compare measurements and implicit estimates of cross-shock potential for a quasi-perpendicular weak (low Mach) shock and a quasi-perpendicular strong (moderate/high Mach) shock using data from the four Magnetospheric Multiscale satellites. The weak shock had lower cross-shock potential in the Normal Incidence Frame (about 30 V) than the strong shock (about 300 V). We also estimated the potential deduced from ion and electron data. Electron-based estimates agreed reasonably well with the measurements, but ion-based estimates encountered problems. The weak shock was too short compared to the ion data sampling period, while the strong shock reflected ions back into the upstream flow. Data from individual spacecraft indicated that the surface of the strong shock was not flat but rippled, one reason why its measured potential showed such a broad range.

1. Introduction

The electric cross-shock potential is an important element of shock structure, influencing energy redistribution at the shock front (Zank et al., 1996). The potential difference, its distribution across the shock, and the scale of its variation are of primary importance for understanding physical processes in shocks. Goodrich and Scudder (2016) were the first to point out the dependence of potential field on the reference frame and to highlight the role of the potential in the formation of flattop and beam-like characteristics of the electron distribution.

Collisionless shocks have been studied for over 60 years, and many satellites have collected in situ measurements of interplanetary (IP) shocks and Earth's bow shock (International Sun-Earth Explorer (ISEE), Sckopke et al., 2010; Cluster and Time History of Events and Macroscale Interactions during Substorms (THEMIS), Hobara et al., 2010; Polar, Hull et al., 2006; Wind, Wilson et al., 2012). Significant progress has been made in understanding the mechanisms of energy transformation from the directed ion flow to the thermal and suprathermal populations (see reviews by Bale et al., 2005; Krasnoselskikh et al., 2013, and references therein). The structure of the magnetic field shock front; evolution of ion and electron distribution functions; and characteristics of waves upstream, inside, and downstream of the shock have been reported in numerous publications (Krasnoselskikh et al., 2013). However, there are only a few publications devoted to measurements of electric field and electrostatic potential across the shock (Bale

et al., 2008; Bale & Mozer, 2007; M. Balikhin et al., 2005; M. A. Balikhin et al., 2002; Dimmock et al., 2011, 2012; Formisano, 1982; Heppner et al., 1984; Hobara et al., 1978; Scudder, Mangeney, Lacombe, Harvey, Aggson, Anderson, et al., 1986; Scudder, Mangeney, Lacombe, Harvey, & Aggson, 1986; Scudder, Mangeney, Lacombe, Harvey, Wu, et al., 1986; Walker et al., 2004; Wygant et al., 1987). One reason for the scarcity of electric field data is associated with the difficulty of the measurement.

Three methods to handle measurements of the electric field were discussed by Dimmock et al. (2011). The first is to neglect the effects of the spin-axis component by projecting the spin-plane measurements onto the shock normal. This allows evaluation of the field and electrostatic potential when the rotation axis is close to the magnetic field direction. Two other techniques rely on reconstructing the spin-axis component based on assumptions about the electric field structure.

The second technique requires that the electric field component parallel to the magnetic field is zero. In contrast, the third technique supposes that the Normal Incidence Frame (NIF) electric field consists of only two contributions: one from $\boldsymbol{v} \times \boldsymbol{B}$, which is supposed to be constant along the shock crossing, and the other from the electric field along the shock normal. The shock is assumed both planar and stationary, implying that only the magnetic field component perpendicular to the shock normal (i.e., $\boldsymbol{B} \times \boldsymbol{n}$) contributes to $\boldsymbol{v} \times \boldsymbol{B}$, leading to the requirement $\boldsymbol{E} \cdot (\boldsymbol{B} \times \boldsymbol{n}) = 0$. Dimmock et al. (2011) applied all three techniques to a single shock and reached the surprising conclusion that the different techniques yielded similar values of the potential.

There is also an indirect approach for evaluating the electrostatic potential, based on a theoretical hydrodynamic description of the shock, assuming planarity, stationarity, and no reflected ions. These assumptions are suitable for subcritical, low-Mach shocks. With the additional assumption that the shock transition is smaller than the ion inertial length, in agreement with statistical studies by Hobara et al. (2010) and Mazelle et al. (2010), one can derive simplified proxies for the potential. These proxies are based on ion deceleration, which is mainly determined by the potential in the NIF. Another proxy may be found from a simplified description of electron dynamics, neglecting the electron mass.

Hereafter we discuss two high-beta, quasi-perpendicular shocks with multipoint observations from the Magnetospheric Multiscale (MMS) mission. MMS is a four-spacecraft constellation, flying in a tetrahedral formation with typical separation distances of tens of kilometers (Fuselier et al., 2016). The primary science goal of MMS is to investigate reconnection processes, but the wealth of data provides ample material for the study of other space plasma phenomena. One of our events of interest is a planar IP shock with low Mach number, and the other is a rippled bow shock crossing with moderate Mach number. For both events, we compare the cross-shock potential profiles obtained from the measurements to proxies computed from the magnetic field data and particle moments.

2. Characteristic Parameters and Data Overview

Collisionless shocks in space plasma are characterized by several parameters, computed upstream of the shock, that determine their scales and general behavior:

1. the angle θ_{Bn} of the shock normal relative to the background magnetic field;
2. magnetosonic Mach number M_F, the ratio of the flow speed to the characteristic speed of fast magnetosonic waves propagating at angle θ_{Bn} relative to the background magnetic field;
3. ion and electron β, the ratio of particle pressure to magnetic field pressure; and
4. the ratio of the Alfvén speed v_A to the speed of light c, $v_A/c = \Omega_i/\omega_i$, where Ω_i and ω_i are the ion gyrofrequency and plasma frequency, respectively.

These parameters form the basis of shock classification. In particular, shocks are divided into two main groups: quasi-perpendicular ($60° < \theta_{Bn} < 90°$), quasi-parallel ($\theta_{Bn} < 40°$), and intermediate (θ_{Bn} between these extremes). A shock may be considered fully perpendicular if $\cos(\theta_{Bn})$ is less than the ratio of electron to ion mass. These limits are not precisely determined. Rather, they are based on the trajectories of particles reflected from the shock front. In quasi-parallel shocks, the reflected particles can infiltrate the upstream flow, whereas in quasi-perpendicular shocks they return to the shock front and eventually cross it.

We present two shocks observed by the four MMS spacecraft: an IP shock with low Mach number observed on 8 January 2018 and the other is a bow shock crossing with moderate Mach number on 2 November 2017.

Magnetic field measurements were obtained from the Fluxgate Magnetometer (FGM; Torbert et al., 2016), and particle data come from the Fast Plasma Investigation (Pollock et al., 2016). While we have performed the analysis using velocity data from both ions and electrons, we ultimately chose the electron velocity because it is more accurately measured in the solar wind. We used spin-plane electric field measurements (Lindqvist et al., 2016) from three of the MMS spacecraft: MMS 1, 2, and 3. The third component of the electric field was reconstructed from $\boldsymbol{E}\cdot\boldsymbol{B}=0$ or $\boldsymbol{E}_{\mathbf{NIF}}\cdot(\boldsymbol{B}\times\boldsymbol{n})=0$ (Dimmock et al., 2011). Additional analysis of the IP shock utilizes magnetic field measurements from the FGMs (Auster et al., 2008) on board the two ARTEMIS spacecraft (Angelopoulos, 2011).

No cleaning or filtering was applied to the magnetic field data. The IP shock electron velocity data were sufficiently clean, but the electron velocity data for the bow shock crossing were subjected to low-pass filtering to remove high-frequency fluctuations.

Offsets were applied to the electric field components such that each agreed overall with the features of the solar wind $\boldsymbol{v}\times\boldsymbol{B}$. This electric field data were later used to calculate the cross-shock potentials. We also obtained shock normals from the bow shock electric fields after band-pass filtering.

Oscillations in the form of precursor whistlers and statistical fluctuations in the ion moments are present in the data of both shocks before and after the ramp. Whistlers do not impact the shock geometry, and any effect they have on electrostatic potential occurs outside the ramp. Ion moment fluctuations surrounding the IP shock and preceding the bow shock crossing are most probably spacecraft orientation effects caused by the nonspecific Fast Plasma Investigation measurement regime in the solar wind. The periodic spikes visible in the IP shock electric field fortunately land on either side of the ramp (the spikes are due to wake effects, which can be mitigated by the algorithm of (Eriksson et al., 2007); see the dotted trace in Figure 1c). Finally, in order to shift the electric field from the spacecraft frame to the NI frame, the shock-tangential components of the transformation velocity are obtained from averages of the upstream electron velocity data, which has better statistics in the solar wind and should minimize the effect of oscillations.

2.1. IP shock

An IP shock swept past all four MMS spacecraft simultaneously on 8 January 2018/06:41:11, while the spacecraft were separated by 15–24 km at [4.3, 22.7, −0.6] (Geocentric Solar Magnetic (GSM) coordinates in R_E). An overview of the data is shown in Figures 1a–1f. (Additional plot of magnetic field components and detailed table of average plasma parameters are included in the supporting information). The IP shock had $\theta_{Bn}=(69\pm2)^{\circ}$, $\beta_i=2.8\pm0.4$, $\beta_e=2.29\pm0.02$, Alfvén ratio $(1.34\pm0.01)\times10^{-4}$, and $M_F=1.1\pm0.1$. (However, the upstream ion temperature is likely overestimated by MMS. Ion temperature data from Wind is more reliable and instead yields $\beta_i=0.3\pm0.1$ and $M_F=1.5\pm0.2$, close to the subcritical value.)

We determined the shock normal in two ways: minimum variance analysis (MVA) and timing analysis of the data from the four satellites. MVA was performed on the magnetic field data from each spacecraft (8 January 2018/06:41:07.5–14.5). All MVA shock normals were within 10° of the timing analysis shock normal and nearly identical (in the context of the error cone) to each other (see supporting information for details). The second direction of the full set of basis vectors was obtained by projecting the MMS3 average upstream magnetic field onto the plane perpendicular to the shock normal, while the third direction completed the right-handed set.

2.2. Bow Shock Crossing

MMS passed from the solar wind through the bow shock around 04:26:46 on 2 November 2017. At this time, the spacecraft were separated by 23–30 km at [24.2, 1.7, 7.0] (GSM coordinates in R_E). An overview of the data is shown in Figures 1g–1l. All four spacecraft passed together through the ramp. (See plot of magnetic field components and detailed table of average plasma parameters in the supporting information). The bow shock crossing had $\theta_{Bn}=(85\pm5)^{\circ}$, $\beta_i=1.4\pm0.2$, $\beta_e=1.4\pm0.1$, Alfvén ratio $(2.1\pm0.1)\times10^{-4}$, and $M_F=2.13\pm0.04$.

To estimate the local geometry of the shock surface, maximum variance analysis was performed on the band-pass-filtered electric field data from each spacecraft during the ramp. The results showed significant deviation from the timing analysis normal, presumably indicating that the shock surface is rippled. MVA on the magnetic field data was unsuccessful (the intermediate and minimum variance components were comparable) because of the significant thickness of the shock structure and strong perturbations in the upstream magnetic field (see supporting information for details).

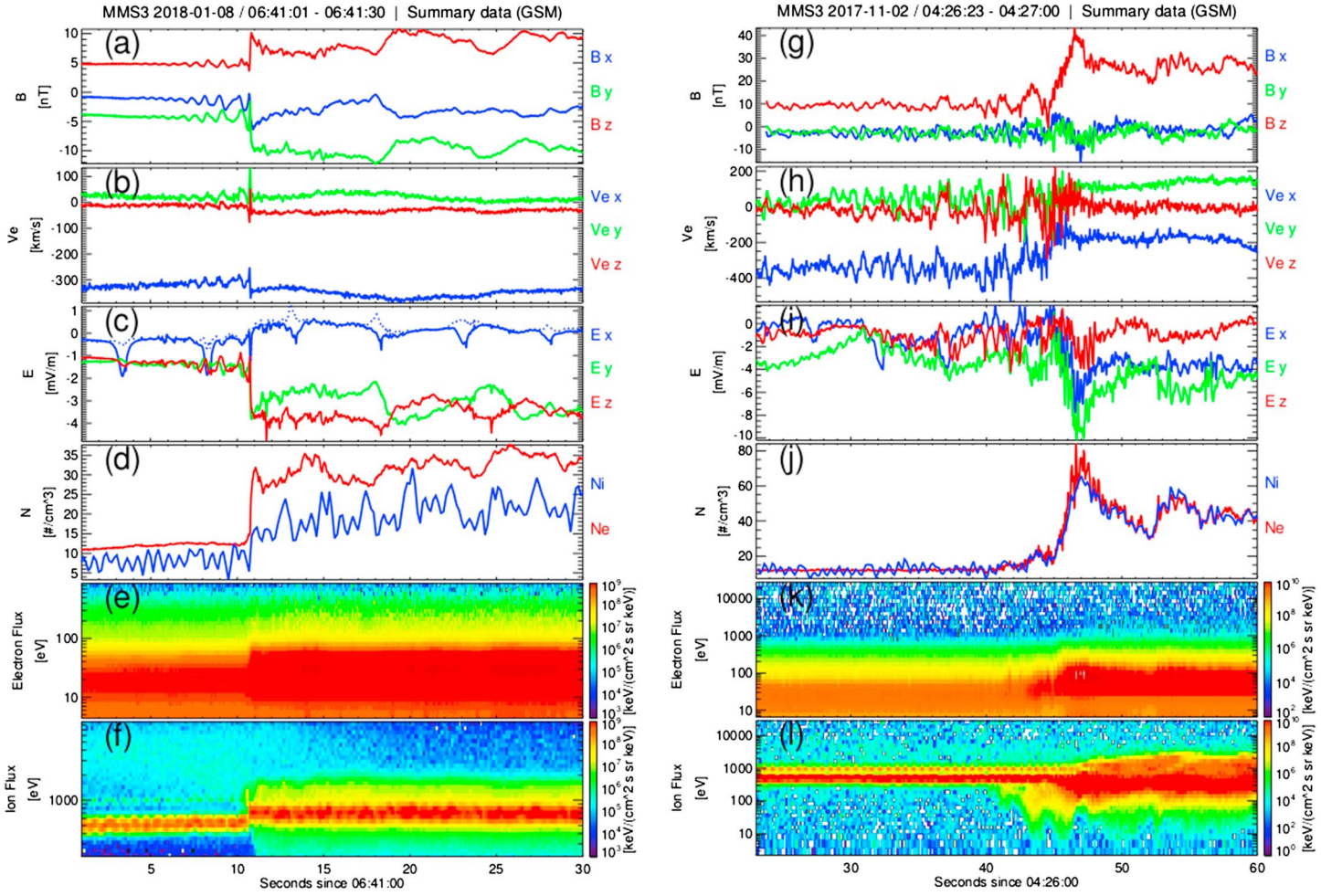

Figure 1. Summary of MMS3 data for (a–f) interplanetary shock on 8 January 2018 and (g–l) bow shock crossing on 2 November 2017. (a, g) Magnetic field (GSM). (b, h) Electron velocity (GSM). (c, i) Electric field (GSM). (d, j) Ion and electron densities. (e, k) Ion energy flux. (f, l) Electron energy flux. MMS = Magnetospheric Multiscale; FGM = Fluxgate Magnetometer.

We opted to use the timing analysis shock normal, with the full set of basis vectors defined in the same way as for the IP shock. The MMS3 upstream magnetic field provided the second direction of the MVA coordinate system because the MMS3 individual shock normal agreed well with the timing analysis result. The magnetic field, filtered electron velocity, and unfiltered electric field data were all rotated into this coordinate system.

3. Cross-Shock Potential

3.1. Estimating the Cross-Shock Potential From Electric Field Measurements

The cross-shock potential was estimated first in the NIF, where the shock front is at rest and the upstream bulk flow is normal to the shock. The shock velocity becomes the shock normal component of the transformation velocity, while the components tangent to the shock surface are the average components of the upstream electron velocity. The electron velocity and electric field transform accordingly:

$$\boldsymbol{v}_{NI} = \boldsymbol{v}_{MVA} - \boldsymbol{v}_{T,NI},$$
$$\boldsymbol{E}_{NI} = \boldsymbol{E}_{MVA} + \boldsymbol{v}_{T,NI} \times \boldsymbol{B},$$

where $\boldsymbol{v}_{T,\,\mathrm{NI}}$ is the constant transformation velocity and the electric field is unfiltered.

We integrated the shock normal component of the electric field over the ramp, obtaining cross-shock potentials for both shocks (see Table S5 in the supporting information for details). Two reconstructions of the

MMS3 electric field were applied: $\boldsymbol{E}\cdot\boldsymbol{B}=0$ and $\boldsymbol{E}_{\mathrm{NIF}}\cdot(\boldsymbol{B}\times\boldsymbol{n})=0$ (Dimmock et al., 2011), although strictly speaking the latter is only expected to be valid for low-Mach shocks. However, even for the IP shock, the second reconstruction was hindered by the shock geometry: because the magnetic field is often aligned with the spacecraft axis, solving for the electric field axial component can lead to division by numbers near zero. Unrealistically large fluctuations are the result, with a cross-shock potential at least twice as large as the value obtained by assuming $\boldsymbol{E}\cdot\boldsymbol{B}=0$. Thus, while the technique is theoretically well justified (Dimmock et al., 2011), we found it inapplicable in our study, yielding unrealistic electric field magnitudes due to the natural constraints of the inversion procedure. Therefore, we only show the potentials from $\boldsymbol{E}\cdot\boldsymbol{B}=0$.

We also attempted to transform the data from the spacecraft frame to the HT frame, using the procedure outlined in section 9.3.1 of Khrabrov and Sonnerup (1998). While this transformation minimizes the motional electric field in the upstream region, in the shock ramp the potential due to the motional electric field exceeds the potential of the measured electric field, and we did not pursue the transformation further. However, examination of the magnetic field-aligned electron distributions can often provide an alternative estimate of the HT frame potential (Lefebvre et al., 2007).

3.2. Potential Proxies From Moments and Magnetic Field

We computed four proxies of the electric potential (Gedalin & Balikhin, 2004):

$$\Phi_v = 1-v_i^2/\langle v_{i,up}\rangle^2,$$

$$\Phi_n = 1-\langle n_{i,up}\rangle^2/n_i^2,$$

$$\Phi_P = 1-\left(1-\frac{\left(P_i-\langle P_{i,up}\rangle\right)+\left(P_e-\langle P_{e,up}\rangle\right)+\left(B^2-\langle B_{up}\rangle^2\right)/2\mu_0}{m_i\langle n_{i,up}\rangle\langle v_{i,up}\rangle^2}\right)^2$$

$$\Phi_e = \frac{-1}{e}\int\frac{1}{n_i}\frac{\partial}{\partial z}\left[\frac{B_x^2+B_y^2}{2\mu_0}+P_e\right]dz.$$

In the above equations, Φ_v is derived from ion velocity, Φ_n from ion density, Φ_P from balancing thermal and magnetic pressures, and Φ_e from the electron equation of motion. Thus, v_i is ion velocity along the shock normal, n_i is ion density, P_i is ion thermal pressure, P_e is electron thermal pressure, B is magnetic field magnitude, m_i is ion mass, e is positive elementary charge, and B_x and B_y are the magnetic field components perpendicular to the shock normal. Averaged quantities $\langle X_{up}\rangle$ are computed upstream.

3.3. IP Shock

Timing analysis provided a shock velocity of (330 ± 30) km/s in the spacecraft frame. The shock ramp passed over MMS3 in 0.1 s. From this, we found the length of the shock crossing to be (33 ± 3) km, smaller than the ion inertial length of about (69 ± 1) km.

Figures 2a–2d shows the MMS3 proxies and potential (similar plots for MMS1 and MMS2 are available in the supporting information). The reflected ions (accelerated to ~3–7 keV) seen upstream in Figure 1e comprise less than 0.05 of the total ion density and thus do not spoil the ion proxies. Their density slowly decays in the upstream direction, and reflected ions are seen at distances up to 8 R_E ahead of the shock. This indicates a large-scale planarity of the IP shock. The IP shock velocity and planar geometry were confirmed on the large scale (~60 R_E) by ARTEMIS (THB and THC spacecraft) measurements in a vicinity of the Moon. THB was at [−8.9, −57.1, 4.2] (Geocentric Solar Ecliptic (GSE) coordinates in R_E) and observed the IP shock crossing at 06:50:09 (see Figure S4 in the supporting information). THC was at [−7.1, −58.8, 4.5] and observed the IP shock crossing at 06:49:53.

The extreme brevity of the shock crossing prevents us from drawing conclusions about the proxies dependent upon ion moments, which have a sampling period similar to the ramp observation. The proxy in Figure 2c depends only on electron moments and shows a flat approach to and smooth increase during the ramp, on the order of (42 ± 10) V. The observed NIF potential in Figure 2d is roughly (24 ± 6) V for MMS3. A similar trend is apparent for MMS1 and MMS2 (see Table S5 in the supporting information).

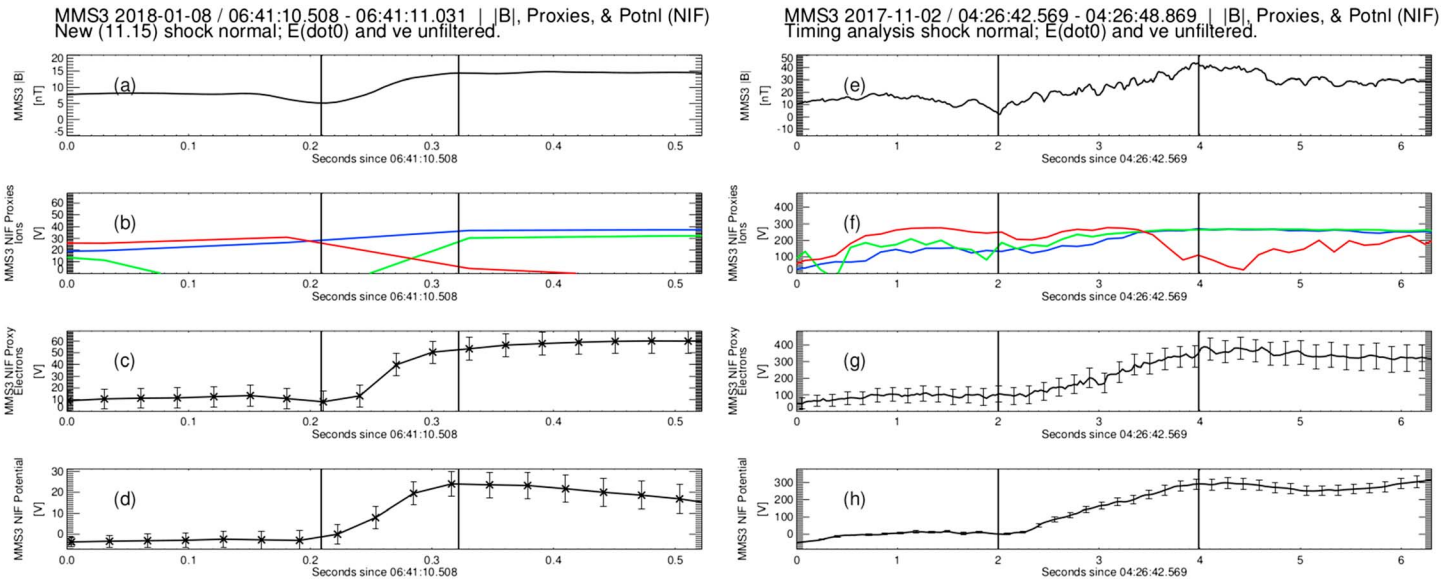

Figure 2. MMS3 magnetic field magnitude, potential proxies, and cross-shock potential for (a–d) interplanetary shock on 8 January 2018 and (e–h) bow shock crossing on 2 November 2017. The ramp is marked by vertical lines through all panels. (a, e) Magnetic field magnitude. (b, f) Potential proxies that depend on ion moments: Φ_v from ion velocity (blue), Φ_n from ion density (green), and Φ_P from pressure balance (red). Note that Φ_P depends on the pressure due to electrons as well as ions. (c, g) Potential proxy that does not depend on ion moments: Φ_e from electron equation of motion. (d, h) Cross-shock potential in NIF. Error bars for all points are shown in (c) and (d). For the sake of visual clarity, error bars for only one fifth of the points in (g) and (h) are shown. MMS = Magnetospheric Multiscale; NIF = Normal Incidence Frame.

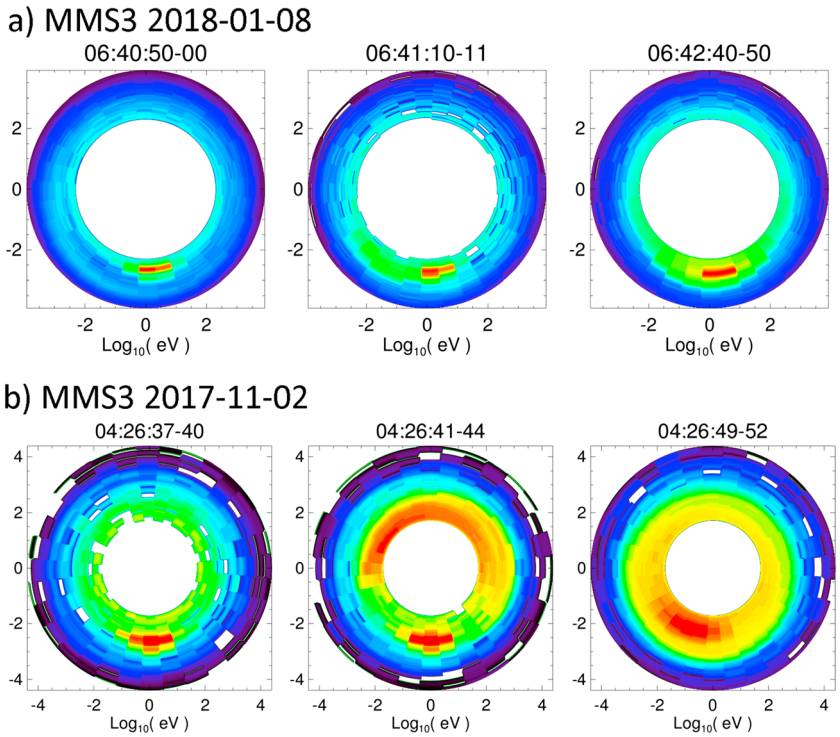

Figure 3. The MMS3 ion distributions in energy and azimuthal angle for (a) interplanetary shock crossing on 8 January 2018 and (b) bow shock crossing on 2 November 2017. Time ranges shown are upstream (left), spanning the interpla netary shock ramp or just preceding the bow shock ramp (center), and downstream (right). MMS = Magnetospheric Multiscale.

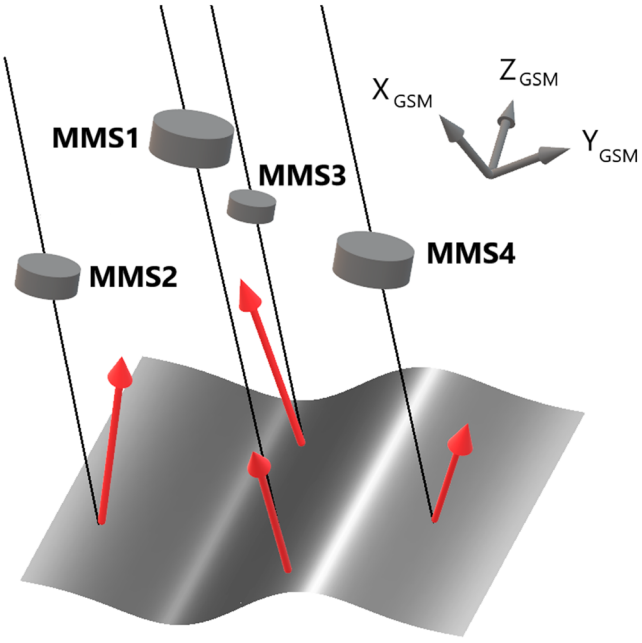

Figure 4. Shock geometry. The shock normal vectors from minimum variance analysis of electric field data are shown for MMS1–MMS4; the shaded surface is a sketch reconciling the shock normals by means of a rippled front. The dominant magnetic field direction approximately coincides with GSM ***Z***. The MMS4 shock normal is estimated from spin rate electric field data. MMS = Magnetospheric Multiscale.

3.4. Bow Shock

The NIF potentials varied between 290 and 440 V for the different spacecraft measurements (see Table S5 in the supporting information). The field-aligned electron distributions allowed estimation of the HT frame potential: the width of the flattop downstream corresponded to a potential of about (150 ± 20) V.

The shock velocity from timing analysis was (60 ± 10) km/s in the spacecraft frame, and the ramp passed over MMS3 in approximately 2 s giving an approximate shock length of (120 ± 20) km. Although this is larger than the ion inertial length of about (65 ± 1) km, we computed potential proxies for this event as well. Before discussing the proxies, it is important to point out some features of the ion distributions. Figure 3b shows ion distributions measured by MMS3 at the bow shock, with two slices before (upstream) and one slice after (downstream) the shock ramp. The coordinate system is centered on the spacecraft. The ions are effectively demagnetized and their motion is stable with respect to the spacecraft. All polar angles have been combined; the angular position in the plot represents azimuthal angle in the spin plane.

In the far-upstream distribution of Figure 3b, the solar wind is visible as a concentrated beam in energy and angle. The near-upstream distribution, showing a time range shortly before the ramp, shows not only the localized solar wind beam but also a lower-energy population traveling in the opposite direction with large angular spread. These are ions reflected from the positive electrostatic potential in the shock front. In the downstream plot, ions are observed at all angles and lower energies, indicating that they have been decelerated while passing through the ramp.

For comparison, the ion distributions from the IP shock are plotted in Figure 3a. The lowest available energy bin for the IP shock distributions was around 200 eV because the four spacecraft were operating in solar wind mode. The time ranges shown are upstream, spanning the ramp, and downstream. No clear indication of reflected ions is seen, but the energy cutoff may introduce some uncertainty.

Figures 2e–2h shows the proxies and potential from MMS3 for the bow shock crossing. (Similar plots for MMS1 and MMS2 are available in the supporting information). The detrimental influence of reflected ions during 04:26:41–44 is clearly visible as enhancements in the potential proxies of Figure 2f, all of which depend on ion moments. The pressure balance proxy, which depends upon both ions and electrons and is displayed with the ion proxies in Figure 2f, is also significantly disturbed downstream of the shock. This is due to downstream electrons reflecting off the shock ramp. In contrast, the proxy determined by the electron equation of motion in Figure 2g shows a flat approach to the ramp and a smooth increase on the order of (250 ± 60) V. The observed NIF potential in Figure 2h is roughly (290 ± 30) V.

4. Discussion and Conclusions

The most striking difference between the low and high Mach number shocks was the geometry of the shock surface. The low Mach number IP shock was almost planar on the scale of the MMS interspacecraft separation, with the individual normals deviating from the timing normal by less than 10°. In contrast, the high Mach number bow shock exhibited a perturbed surface that was rippled on the scale of the MMS spacecraft configuration. Individual normals deviated from the timing analysis normal by up to 30°. This is presumably a typical feature of high Mach number shocks, in agreement with several past modeling studies of shocks (Burgess, 2006; Burgess & Scholer, 2007; Lowe & Burgess, 2003; Ofman & Gedalin, 2013a, 2013b; Winske & Quest, 1988) as well as observations reported by (Johlander et al., 2016). In particular, Ofman and Gedalin (2013a, 2013b) discussed the deviation of the shock normal due to rippling, based on their 2-D hybrid simulation study. The geometry of our observations is sketched in Figure 4, which shows the bow

shock surface, with the electric field MVA normal in red at each spacecraft. A ripple in the shock surface helps reconcile the individual normals.

To conclude, we present the results of a comparative study of two quasi-perpendicular collisionless shocks in the solar wind, with low (IP shock) and high (bow shock) Mach number:

1. The cross-shock NIF potential from electric field measurements is 24–28 V for the IP shock (with 41–42 V from the electron proxies), and 290–440 V for the bow shock (with 240–260 V from the electron proxies).
2. The ion proxies cannot be used for high Mach number shocks because the ion moments are spoiled by reflected ions before and during the ramp.
3. The low Mach number IP shock surface was almost planar on the scale of the MMS spacecraft configuration as well as on the scale of the MMS and ARTEMIS separation distance (~20 R_E).
4. The high Mach number bow shock surface was rippled on the scale of the MMS spacecraft configuration, in agreement with the results of Burgess (2006), Burgess and Scholer (2007), Lowe and Burgess (2003), Ofman and Gedalin (2013a, 2013b), and Winske and Quest (1988) and the observations of Johlander et al. (2016).

Acknowledgments
The authors thank the entire MMS team for providing such excellent data, which is publicly available (https://lasp.colorado.edu/mms/sdc/public/about/how-to/). The authors thank C. T. Russell, S. J. Schwartz, and R. B. Torbert for fruitful discussion and valuable comments. E. H. acknowledges the support of NESSF grant HELIO17R-0008. The work by O. A. and F. M. was performed under THEMIS NASA contract NAS5-02099, NASA 80NSSC18K0155 contract, and JHU/APL contract 922613 (RBSP-EFW). V. K. was supported by the STEREO-WAVES Invited Scientist grant. The authors acknowledge NASA contract NAS5-02099 and V. Angelopoulos for use of data from the THEMIS Mission and K. H. Glassmeier, U. Auster, and W. Baumjohann for the use of FGM data provided under the lead of the Technical University of Braunschweig and with financial support through the German Ministry for Economy and Technology and the German Center for Aviation and Space (DLR) under contract 50 OC 0302.

References

Angelopoulos, V. (2011). The ARTEMIS mission. *Space Science Reviews*, *165*(1–4), 3–25. https://doi.org/10.1007/s11214-010-9687-2

Auster, H. U., Glassmeier, K. H., Magnes, W., Aydogar, O., Baumjohann, W., et al. (2008). The THEMIS fluxgate magnetometer. *Space Science Reviews*, *141*(1–4), 235–264. https://doi.org/10.1007/s11214-008-9365-9

Bale, S. D., Balikhin, M. A., Horbury, T. S., Krasnoselskikh, V. V., Kucharek, H., Möbius, E., et al. (2005). Quasi-perpendicular Shock Structure and Processes. *Space Science Reviews*, *118*(1–4), 161–203. https://doi.org/10.1007/s11214-005-3827-0

Bale, S. D., & Mozer, F. S. (2007). Measurement of Large Parallel and Perpendicular Electric Fields on Electron Spatial Scales in the Terrestrial Bow Shock. *Physical Review Letters*, *98*(20). https://doi.org/10.1103/PhysRevLett.98.205001

Bale, S. D., Mozer, F. S., & Krasnoselskikh, V. V. (2008). Direct measurement of the cross-shock electric potential at low plasma β, quasi-perpendicular bow shocks. *ArXiv:0809.2435 [Astro-Ph, Physics:Physics]*. Retrieved from http://arxiv.org/abs/0809.2435

Balikhin, M., Walker, S., Treumann, R., Alleyne, H., Krasnoselskikh, V., Gedalin, M., et al. (2005). Ion sound wave packets at the quasi-perpendicular shock front. *Geophysical Research Letters*, *32*, L24106. https://doi.org/10.1029/2005GL024660

Balikhin, M. A., Nozdrachev, M., Dunlop, M., Krasnosel'skikh, V., Walker, S. N., Alleyne, H. S. C. K., et al. (2002). Observation of the terrestrial bow shock in quasi-electrostatic subshock regime. *Journal of Geophysical Research*, *107*(A8), 1155. https://doi.org/10.1029/2001JA000327

Burgess, D. (2006). Simulations of electron acceleration at collisionless shocks: The effects of surface fluctuations. *The Astrophysical Journal*, *653*(1), 316–324. https://doi.org/10.1086/508805

Burgess, D., & Scholer, M. (2007). Shock front instability associated with reflected ions at the perpendicular shock. *Physics of Plasmas*, *14*(1), 012108. https://doi.org/10.1063/1.2435317

Dimmock, A. P., Balikhin, M. A., Krasnoselskikh, V. V., Walker, S. N., Bale, S. D., & Hobara, Y. (2012). A statistical study of the cross-shock electric potential at low Mach number, quasi-perpendicular bow shock crossings using Cluster data. *Journal of Geophysical Research*, *117*, A02210. https://doi.org/10.1029/2011JA017089

Dimmock, A. P., Balikhin, M. A., & Hobara, Y. (2011). Comparison of three methods for the estimation of cross-shock electric potential using Cluster data. *Annales Geophysicae*, *29*(5), 815–822. https://doi.org/10.5194/angeo-29-815-2011

Eriksson, A. I., Khotyaintsev, Y., & Lindqvist, P.-A. (2007). Spacecraft wakes in the solar wind. In *Proceedings of the 10th Spacecraft Charging Technology Conference* (14 pp.).

Formisano, V. (1982). Measurement of the potential drop across the Earth's collisionless bow shock. *Geophysical Research Letters*, *9*(9), 1033–1036. https://doi.org/10.1029/GL009i009p01033

Fuselier, S. A., Lewis, W. S., Schiff, C., Ergun, R., Burch, J. L., Petrinec, S. M., & Trattner, K. J. (2016). Magnetospheric Multiscale Science Mission Profile and Operations. *Space Science Reviews*, *199*(1–4), 77–103. https://doi.org/10.1007/s11214-014-0087-x

Gedalin, M., & Balikhin, M. (2004). Electric potential in the low-Mach-number quasi-perpendicular collisionless shock ramp revisited. *Journal of Geophysical Research*, *109*, A03106. https://doi.org/10.1029/2003JA010219

Goodrich, C. C., & Scudder, J. D. (1984). The adiabatic energy change of plasma electrons and the frame dependence of the cross-shock potential at collisionless magnetosonic shock waves. *Journal of Geophysical Research*, *89*(A8), 6654–6662. https://doi.org/10.1029/JA089iA08p06654

Heppner, J. P., Maynard, N. C., & Aggson, T. L. (1978). Early results from ISEE-1 electric field measurements. *Space Science Reviews*, *22*(6), 777–789. https://doi.org/10.1007/BF00212623

Hobara, Y., Balikhin, M., Krasnoselskikh, V., Gedalin, M., & Yamagishi, H. (2010). Statistical study of the quasi-perpendicular shock ramp widths. *Journal of Geophysical Research*, *115*, A11106. https://doi.org/10.1029/2010JA015659

Hull, A. J., Larson, D. E., Wilber, M., Scudder, J. D., Mozer, F. S., Russell, C. T., & Bale, S. D. (2006). Large-amplitude electrostatic waves associated with magnetic ramp substructure at Earth's bow shock. *Geophysical Research Letters*, *33*, L15104. https://doi.org/10.1029/2005GL025564

Johlander, A., Schwartz, S. J., Vaivads, A., Khotyaintsev, Y. V., Gingell, I., Peng, I. B., et al. (2016). Rippled quasiperpendicular shock observed by the Magnetospheric Multiscale Spacecraft. *Physical Review Letters*, *117*(16), 165101. https://doi.org/10.1103/PhysRevLett.117.165101

Khrabrov, A. V., & Sonnerup, B. U. Ö. (1998). De Hoffmann-Teller analysis. In G. Paschmann & P. W. Daly (Eds.), *Analysis methods for multi-spacecraft data, International Space Science Institute Scientific Report SR-001* (pp. 221–248). Noordwijk, Netherlands: ESA Publications Division.

Krasnoselskikh, V., Balikhin, M., Walker, S. N., Schwartz, S., Sundkvist, D., Lobzin, V., et al. (2013). The Dynamic Quasiperpendicular Shock: Cluster Discoveries. *Space Science Reviews*, *178*(2–4), 535–598. https://doi.org/10.1007/s11214-013-9972-y

Lefebvre, B., Schwartz, S. J., Fazakerley, A. F., & Décréau, P. (2007). Electron dynamics and cross-shock potential at the quasi-perpendicular Earth's bow shock. *Journal of Geophysical Research*, *112*, A09212. https://doi.org/10.1029/2007JA012277

Lindqvist, P.-A., Olsson, G., Torbert, R. B., King, B., Granoff, M., Rau, D., et al. (2016). The spin-plane double probe electric field instrument for MMS. *Space Science Reviews*, *199*(1–4), 137–165. https://doi.org/10.1007/s11214-014-0116-9

Lowe, R. E., & Burgess, D. (2003). The properties and causes of rippling in quasi-perpendicular collisionless shock fronts. *Annales Geophysicae*, *21*(3), 671–679. https://doi.org/10.5194/angeo-21-671-2003

Mazelle, C., Lembège, B., Morgenthaler, A., Meziane, K., Horbury, T. S., Génot, V., et al. (2010). Self-Reformation of the Quasi-Perpendicular Shock: CLUSTER Observations. In *Presented at the Twelfth International Solar Wind Conference* (pp. 471–474). Saint-Malo, France. https://doi.org/10.1063/1.3395905

Ofman, L., & Gedalin, M. (2013a). Rippled quasi-perpendicular collisionless shocks: Local and global normals. *Journal of Geophysical Research: Space Physics*, *118*, 5999–6006. https://doi.org/10.1002/2013JA018780

Ofman, L., & Gedalin, M. (2013b). Two-dimensional hybrid simulations of quasi-perpendicular collisionless shock dynamics: Gyrating downstream ion distributions. *Journal of Geophysical Research: Space Physics*, *118*, 1828–1836. https://doi.org/10.1029/2012JA018188

Pollock, C., Moore, T., Jacques, A., Burch, J., Gliese, U., Saito, Y., et al. (2016). Fast plasma investigation for magnetospheric multiscale. *Space Science Reviews*, *199*(1–4), 331–406. https://doi.org/10.1007/s11214-016-0245-4

Sckopke, N., Paschmann, G., Bame, S. J., Gosling, J. T., & Russell, C. T. (1983). Evolution of ion distributions across the nearly perpendicular bow shock: Specularly and non-specularly reflected-gyrating ions. *Journal of Geophysical Research*, *88*(A8), 6121. https://doi.org/10.1029/JA088iA08p06121

Scudder, J. D., Mangeney, A., Lacombe, C., Harvey, C. C., Aggson, T. L., Anderson, R. R., et al. (1986). The resolved layer of a collisionless, high β, supercritical, quasi-perpendicular shock wave: 1. Rankine-Hugoniot geometry, currents, and stationarity. *Journal of Geophysical Research*, *91*(A10), 11019. https://doi.org/10.1029/JA091iA10p11019

Scudder, J. D., Mangeney, A., Lacombe, C., Harvey, C. C., & Aggson, T. L. (1986). The resolved layer of a collisionless, high β, supercritical, quasi-perpendicular shock wave: 2. Dissipative fluid electrodynamics. *Journal of Geophysical Research*, *91*(A10), 11053. https://doi.org/10.1029/JA091iA10p11053

Scudder, J. D., Mangeney, A., Lacombe, C., Harvey, C. C., Wu, C. S., & Anderson, R. R. (1986). The resolved layer of a collisionless, high β, supercritical, quasi-perpendicular shock wave: 3. Vlasov electrodynamics. *Journal of Geophysical Research*, *91*(A10), 11075. https://doi.org/10.1029/JA091iA10p11075

Torbert, R. B., Russell, C. T., Magnes, W., Ergun, R. E., Lindqvist, P.-A., Le Contel, O., et al. (2016). The FIELDS instrument suite on MMS: Scientific objectives, measurements, and data products. *Space Science Reviews*, *199*(1–4), 105–135. https://doi.org/10.1007/s11214-014-0109-8

Walker, S. N., Alleyne, H. S. C. K., Balikhin, M. A., André, M., & Horbury, T. S. (2004). Electric field scales at quasi-perpendicular shocks. *Annales Geophysicae*, *22*(7), 2291–2300. https://doi.org/10.5194/angeo-22-2291-2004

Wilson, L. B., Koval, A., Szabo, A., Breneman, A., Cattell, C. A., Goetz, K., et al. (2012). Observations of electromagnetic whistler precursors at supercritical interplanetary shocks. *Geophysical Research Letters*, *39*, L08109. https://doi.org/10.1029/2012GL051581

Winske, D., & Quest, K. B. (1988). Magnetic field and density fluctuations at perpendicular supercritical collisionless shocks. *Journal of Geophysical Research*, *93*(A9), 9681–9693. https://doi.org/10.1029/JA093iA09p09681

Wygant, J. R., Bensadoun, M., & Mozer, F. S. (1987). Electric field measurements at subcritical, oblique bow shock crossings. *Journal of Geophysical Research*, *92*(A10), 11109. https://doi.org/10.1029/JA092iA10p11109

Zank, G. P., Pauls, H. L., Cairns, I. H., & Webb, G. M. (1996). Interstellar pickup ions and quasi-perpendicular shocks: Implications for the termination shock and interplanetary shocks. *Journal of Geophysical Research*, *101*(A1), 457–477. https://doi.org/10.1029/95JA02860